Photoabsorption of quantum dots in quantum wells with a strong electric bias field

Volkmar Putz, Christopher Ede, and Armin Scrinzi*
Photonics Institute, Vienna University of Technology, Gusshausstrasse 27/387, A-1040 Vienna, Austria
(Received 1 February 2007; revised manuscript received 5 April 2007; published 16 July 2007)

We introduce the resolvent formalism and complex scaling to calculate photoabsorption by transitions from the ground state of a quantum dot embedded in a quantum well to subbands of the well and to the bulk continuum. The method obviates the explicit calculation of continuum states. It is shown that photoabsorption is strongly modified due to distortions of the subband continuum and resonance states induced by the dot potential. An electric bias field causes pronounced modulations of the subband-to-bulk and dot-to-bulk photoabsorption. We explain this behavior by a semiquantitative analytic model.

DOI: 10.1103/PhysRevB.76.035318 PACS number(s): 78.55.Cr, 78.67.Hc

I. INTRODUCTION

Quantum dots (QDs) embedded in semiconductor heterostructures have been studied as one approach to enhancing the efficiency of quantum cascade lasers[1] and for the design of infrared photodetectors.[2–5] Quantum cascade lasers with embedded quantum dots use excited states of the dot as the lasing transitions, for which the longer nonradiative lifetimes of these states compared to subband levels of the well promise higher efficiency. Dot-in-well based infrared photodetectors use transitions from the bound states of the dot into subbands of the surrounding well. The advantages of these devices compared to pure quantum well photodetectors lie in the low dark current due to the $3d$ confinement of the dot states and their sensitivity to normal incidence radiation.

The theoretical modeling of these systems is comparatively simple as only one type of charge carriers is involved. Realistic models of unipolar quantum dots and wells are based on $\vec{k}\cdot\vec{p}$ theory[6–8] or use pseudopotentials.[9] However, even elementary models with only the reduced electron masses and potentials representing the conduction band offsets can reproduce the behavior of such structures qualitatively and also quantitatively.[10] For a model of that type, bound and continuum states of single spherical quantum dots were calculated analytically in Ref. 11. In Ref. 12, infrared photocurrent spectra were investigated by calculating the transition probabilities of electrons trapped in an InAs QD into the subbands of a GaAs cylinder and the influence of resonances in the continuum was studied. In Ref. 13, a theoretical treatment of the bound states in vertically stacked flat dots with electric bias fields was introduced and optical properties such as Stark tunability of the system were described. The electronic continuum states of combined QD/quantum well (QW) systems in magnetic fields were calculated in Ref. 14 using a quasiseparable potential to model flat QDs.

Where analytical solutions are not available, one resorts to numerical solutions of the Schrödinger equation in a finite box. To obtain a dense representation of states near the continuum thresholds, one needs very large box sizes, which make such calculations rather demanding.[14] When an electric bias field is added, a deep "triangular potential" appears at one end of the box, where the highly oscillatory solutions must be carefully calculated in order to obtain the correct continuum structure. Strictly speaking, in the presence of a bias field all bound states dissolve into the continuum as eventually all states will ionize by tunneling. Especially near threshold, no clear distinction between bound states, resonance states, and continuum can be made and formerly bound states may appear only as modulations of the continuum state density. For this reason, three-dimensional calculations for heterostructures have been limited to the (quasi) bound state spectrum.[15–17]

Here, we present calculations of the photoabsorption spectra of quantum wells in a bias field with and without embedded quantum dots in full dimensionality. We introduce exterior complex scaling,[18] which solves the problems related to box size and discretization, gives direct access to resonances embedded in the continuum, and allows the computation of photoabsorption probabilities without explicitly computing continuum states. We find that in the presence of the field, photoabsorption from GaAs/AlGaAs wells strongly oscillates as a function of photon energy and bias field. The behavior is described by a simple analytic model and the same basic model also explains the weaker oscillatory behavior of photoabsorption from an InGaAs quantum dot. Finally, we study transitions from the ground state of the dot into subband continua of a quantum-well heterostructure and into the bulk. The presence of the dot strongly modifies the subband continua and the corresponding photoabsorption spectrum. We show that the field-induced oscillations are independent of the parameters of the heterostructures and can be exploited to directly determine the local bias field across the structure.

II. METHODS

A. Resolvent matrix elements

The photoabsorption cross section from an initial state Ψ_i with energy E_i is proportional to

$$\omega M_i(E) = \omega \sum\!\!\!\!\!\!\int d\alpha |\langle E,\alpha|\vec{\epsilon}\cdot\vec{r}|\Psi_i\rangle|^2, \quad (1)$$

where the summation and integration is over all degenerate final states $|E,\alpha\rangle$ at electron energy $E=\omega+E_i$ with a photon energy of ω. The states are δ normalized $\langle E,\alpha|E',\alpha'\rangle = \delta(E-E')\delta(\alpha-\alpha')$ with respect to energy and α. For the discussion below and for the numerical examples, we restrict

ourselves to light polarizations $\vec{\epsilon}$ and bias fields in the growth (z) direction. However, we will point out straightforward generalizations to arbitrary field directions and polarization. Here and below, we use atomic units $\hbar=4\pi\varepsilon_0=e^2=m_e=1$. The main difficulty in calculating $M_i(E)$ near thresholds arises because the usual plane-wave approximation for continuum states $|E,\alpha\rangle$ is not applicable. In explicit numerical calculations of low energy continuum states, the large de Broglie wavelength requires large box sizes or the imposition of energy-dependent boundary conditions, which is difficult in more than one dimension. Fortunately, the calculation of continuum states can be avoided. Starting from the spectral representation of the system's Green's function,

$$(H-E+i\varepsilon)^{-1}=\sum\!\!\!\!\!\!\int dE' \sum\!\!\!\!\!\!\int d\alpha |E',\alpha\rangle(E-E'+i\varepsilon)^{-1}\langle E',\alpha|, \tag{2}$$

we obtain $M_i(E)$ as the limit of the Green's function matrix element,

$$M_i(E)=-\frac{1}{\pi}\lim_{\varepsilon\to 0}\mathrm{Im}\langle\Psi_i|z\frac{1}{H-E+i\varepsilon}z|\Psi_i\rangle, \tag{3}$$

by observing that

$$\lim_{\varepsilon\to 0}\mathrm{Im}\frac{1}{E'-E+i\varepsilon}=-\pi\delta(E'-E). \tag{4}$$

A straightforward calculation of the limit (3) suffers from the fundamental problem that the resolvent of any discrete approximation of the Hamiltonian has a dense sequence of poles at the energies of the discretized states, where the limit does not exist. The problem can be solved by the analytic continuation technique of complex scaling.[18,19] This method is widely applied in atomic and molecular physics and we give only a brief outline here.

B. Complex scaling

We start from defining the coordinate scaling transformation for real scaling factors a,

$$\Psi_a(\vec{r})=a^{3/2}\Psi(a\vec{r}), \tag{5}$$

which is a unitary transformation due to the factor $a^{3/2}$. A corresponding scaled Hamiltonian operator is obtained by the substitutions of the coordinates and derivatives,

$$H_a=H\left(\vec{r}\to a\vec{r},\vec{\nabla}\to\frac{1}{a}\vec{\nabla}\right). \tag{6}$$

As the scaling transformation is unitary, the spectrum of H_a is the same as the spectrum of H. A formal analytic continuation $a\to\eta$, η complex, is straightforward and leads to the non-Hermitian, "complex scaled" Hamiltonian H_η.[18] Given sufficient analyticity properties of the potential, the analytic continuation of H_η can be made rigorous in the operator sense and it can be shown that bound state energies are analytic functions of η.[20] As an analytic function that is constant on the real axis is constant in the whole complex plane, the invariance of the bound state energies for all real values of $\eta=a$ implies that they remain constant also for *complex* η. However, the continuous spectrum is rotated into the complex plane by the angle -2θ, where $\theta=\arg\eta$. The center of the rotation is at the continuum energy threshold. For the present discussion, it is important that not only the bound state energies but also the matrix elements

$$\langle\Psi_{\eta,L}|\eta z(H_\eta-E+i\varepsilon)^{-1}\eta z|\Psi_{\eta,R}\rangle \tag{7}$$

are analytic functions of η, if the corresponding right and left hand eigenfunctions $\Psi_{\eta,R}$ and $\Psi_{\eta,L}$ of the complex scaled Hamiltonian are used:

$$H_\eta\Psi_{\eta,R}=E_i\Psi_{\eta,R},\quad H_\eta^\dagger\Psi_{\eta,L}^*=E_i\Psi_{\eta,L}^*. \tag{8}$$

Here, $H_\eta^\dagger$ means the adjoint Hamiltonian. By the same argument as for the bound state energies, it follows that the matrix element (7) is independent of η. The advantage of calculating Eq. (7) is that it does not become singular in the limit $\varepsilon\to 0$ as the continuous spectrum of H_η lies in the lower complex half plane. For that reason, efficient discrete approximations of resolvent in Eq. (7) can be found.

The potentials used to describe quantum dots are not, in general, analytic everywhere, e.g., when square-well potentials are used. In that case, it is sufficient to apply the complex scaling transformation only beyond a finite distance,

$$x\to x_0+(x-x_0)\eta\quad\text{for } |x|>x_0>0, \tag{9}$$

and analogously for the coordinates y and z, where different scaling radii x_0, y_0, and z_0 can be chosen for the respective coordinates. In this so-called "exterior complex scaling,"[18] the complex scaled Hamiltonian is only defined on functions that are discontinuous at the scaling radii in the form[19]

$$\Psi(\pm x_0\pm 0)=\eta^{1/2}\Psi(\pm x_0\mp 0). \tag{10}$$

It turns out that the important analyticity of energies and matrix elements is maintained. This allows complex scaled calculations also for potentials that are only analytic beyond a finite region of nonanalyticity.

Another important aspect of complex scaling is that poles of the $\mathcal{S}$ matrix connected to resonances correspond to discrete complex eigenvalues of the scaled Hamiltonian H_η. Such eigenvalues can appear in the wedge-shaped area of the complex plane between the real axis and the rotated continuum. Just like bound states, they are independent of η for all $\arg\eta>\theta_0$ beyond the value θ_0 where they first appear. In numerical calculations, the resonance energies can be identified by their independence of the complex scaling factor η, which distinguishes them from approximate continuum energies that depend on η.

C. Computational aspects

For our calculations, we model the quantum dots and wells in cylindrical symmetry by Hamiltonians of the general form

$$H=-\frac{1}{2m^*(\rho,z)}\left[\frac{1}{\rho}\frac{\partial}{\partial\rho}\rho\frac{\partial}{\partial\rho}+\frac{\partial^2}{\partial z^2}\right]+V(\rho,z)+ezF. \tag{11}$$

Dot and wells are defined through the local effective electron masses $m^*(\rho,z)$ and the potentials $V(\rho,z)$. The bias field F

always points in the z direction. Both the potential and the effective masses are discontinuous at the boundaries between dots, wells, and the bulk material, which introduces well-defined discontinuities into the eigenfunctions of H. The same type of discontinuity is required for exterior complex scaling (10). It is essential for proper convergence of the numerical approximation that these discontinuities are correctly included in the discretization.

The finite element method (FEM) provides a most natural way of including discontinuities into a basis. In FEM, space is divided into a mesh of finite volumes and on each volume the solution is approximated by a polynomial. Usually, the solution is connected continuously across element boundaries. If the element boundary coincides with a discontinuity of the Hamiltonian or a scaling radius, one instead imposes the corresponding condition of *discontinuity*, e.g., Eq. (10).

In our calculations, we use rectangular product grids in the coordinates ρ and z. A FEM approximation to a wave function has the general form

$$\Psi = \sum_{i=1}^{N} c^i |i\rangle, \tag{12}$$

where $|i\rangle = h_{n_i,m_i}(\rho,z)\rangle$ is a polynomial confined to element volume $[\rho_{n_i-1},\rho_{n_i}]\times[z_{m_i-1},z_{m_i}]$. Continuity conditions can be formulated as a linear constraint on the expansion coefficients c_i.[19] The complex scaled Hamiltonian is approximated by the finite matrix

$$\hat{H}_{\eta,ij} = \langle i|H_\eta|j\rangle_\eta, \tag{13}$$

and the unit and dipole operators are approximated by the matrices

$$\hat{S}_{\eta,ij} = \langle i|j\rangle \quad \text{and} \quad \hat{Z}_{\eta,ij} = \langle i|\eta z|j\rangle, \tag{14}$$

respectively. All matrices are restricted to the subspaces with linear constraints corresponding to the proper continuity conditions. The fact that these conditions also depend on η is indicated by the subscript η also for the overlap matrix $\hat{S}_\eta$. The discrete approximation of the resolvent matrix element is given by

$$\langle \Psi_{\eta,L}|\eta z(H_\eta - E)^{-1}\eta z|\Psi_{\eta,R}\rangle \approx c_{\eta,L}\cdot \hat{Z}_\eta(\hat{H}_\eta - E\hat{S}_\eta)^{-1}\hat{Z}_\eta c_{\eta,R}, \tag{15}$$

where the coefficient vectors $c_{\eta,L}$ and $c_{\eta,R}$ fulfill the generalized discrete eigenvalue equations

$$\hat{H}_\eta c_{\eta,R} = \tilde{E}_i \hat{S}_\eta c_{\eta,R}, \quad \hat{H}_\eta^\dagger c_{\eta,L}^* = \tilde{E}_i \hat{S}_\eta^\dagger c_{\eta,L}^*. \tag{16}$$

The eigenvalue $\tilde{E}_i \approx E_i$ is the variational approximation to the exact initial state energy. Note that the dot product in Eq. (15) is defined *without* complex conjugation, which is consistent with the definition of $c_{\eta,L}^*$ in Eq. (16).

One advantage of FEM that it shares with methods such as B-splines or finite differences is its numerical stability. It is also rather easy in FEM to increase the polynomial order p on each element, which usually leads to exponential improvement of accuracy at the expense of an $\sim O(p^3)$ increase in computation times. The mesh sizes are determined by the extension and complexity of the system investigated. As an example, in Table I we show the convergence of photoabsorption from the ground state of a dot-in-well system with a strong bias field of 48 kV. The transition to an energy just below the band edge of the well barrier was selected, as in this case the final state has continuous character in the ρ direction, while it is a decaying state with large decay width in the z direction (see the discussion of Fig. 8). A rather modest number of 420 discretization points suffices for $\sim 1\%$ accuracy. Further details about our implementation of FEM including important aspects of exterior complex scaling can be found in Ref. 19.

TABLE I. Convergence of photoabsorption with the discretization parameters. $M(E)$ from the ground state of a quantum dot embedded in a quantum dot to a subband energy of $E=320$ meV, just below the well barrier conduction band edge. A bias field of 48 kV is applied. System parameters are the same as for Fig. 8. The error $\Delta M/M$ is given with respect to a reference calculation with box size $z\times\rho = 200\times 45$ nm^2 and $n_z\times n_\rho = 799\times 48$ linear discretization coefficients. The order of the FEM polynomials was 4 and 8 in the z and ρ directions, respectively, except for the last two lines, where order 6 was chosen in the ρ direction. The number of elements is approximately equal to the number of coefficients divided by the FEM polynomial order on the respective axis. With only 420 total linear coefficients, 1% accuracy is reached (last line).

n_z	n_ρ	z box (nm)	ρ box (nm)	$\Delta M/M$
399	48	100	30	1.0×10^{-5}
399	48	100	20	5.7×10^{-4}
399	48	100	15	2.3×10^{-2}
199	48	100	30	3.1×10^{-5}
47	48	50	30	2.6×10^{-4}
35	48	50	30	7.2×10^{-3}
199	24	50	20	5.3×10^{-4}
199	12	50	20	2.9×10^{-3}
35	12	50	20	1.0×10^{-2}

Due to the small basis sizes required for discretization, an extension of the method to systems without cylindrical symmetry is straightforward. Photoabsorption with polarizations perpendicular to z can be treated as a first order perturbative process and extending the basis by the dipole-reachable states is sufficient, which would increase the basis sizes by a factor of 3 at most. When stronger static fields significantly break the cylindrical symmetry of the system, the use of Cartesian instead of cylindrical coordinates may be of advantage.

III. ANALYTICAL MODELS

Photoabsorption spectra of quantum wells and dots experience strong modifications in the presence of a bias field. These are caused by the reflection of continuum electrons by the field. In the field direction, the scattering waves have the general character of Airy functions with an energy-dependent sequence of nodes. In good approximation, the photoabsorp-

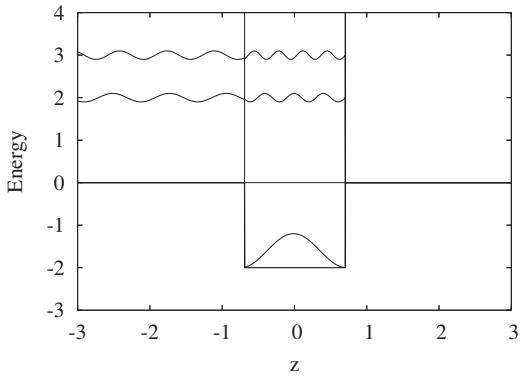

FIG. 1. Square well with a reflecting wall. The symmetric ground state does not dipole connect to excited states that are symmetric above the well, like the lower scattering state shown.

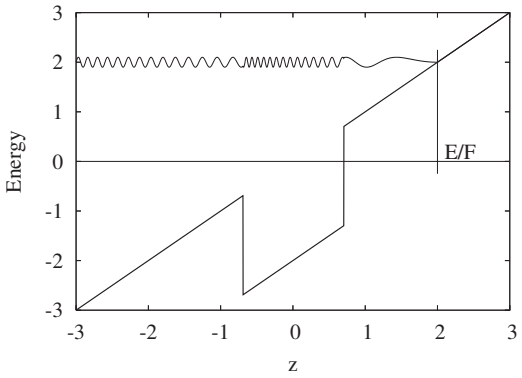

FIG. 2. Well potential with a bias field. A scattering wave of energy E is reflected in the external field F at the classical turning point E/F.

tion spectra can be deduced from simple analytic models.

We first replace the reflection in the bias field by reflection from a rigid wall on one side of a square-well potential. The potential reads

$$\begin{aligned} V(z) &= 0 \quad \text{for} \quad z < -a/2 \\ &= -V_0 \quad \text{for} \quad -a/2 < z < a/2 \\ &= \infty \quad \text{for} \quad a/2 < z. \end{aligned} \tag{17}$$

The continuum solutions in the region of the well are standing waves,

$$\Psi(-a/2 < z < a/2) = C \sin K\left(\frac{a}{2} - z\right),$$

$$K = \sqrt{\frac{2m}{\hbar}(E + V_0)}. \tag{18}$$

The modulus of C depends on energy in the form

$$|C| = \frac{1}{2\sqrt{1 + \frac{V_0}{E}\cos^2 Ka}}, \tag{19}$$

corresponding to Fabry-Pérot-like resonances due to reflections from edges of the well. In addition to this rather smooth variation, the bound-continuum matrix elements periodically change sign with increasing continuum energy, which causes a sequence of zeros in the photoabsorption cross section. For the sake of the argument, we assume that the ground state $|\Psi_i\rangle$ in the well is symmetric with respect to $z=0$ (see Fig. 1). As the continuum energy increases, the character of the continuum wave functions above the well changes from cosinelike and even with respect to $z=0$ to sinelike and odd. With an even initial state dipole transitions to even continuum states are suppressed and photoabsorption goes through a zero.

A. Field-induced modulations

The energy dependence of the spacing between subsequent zeros can be estimated by putting a reflecting wall to an energy-dependent location z_0. A naive choice for z_0 would be the classical turning point of the electron in the bias field $z_0=E/F$ for field strength F (see Fig. 2). This, however, neglects the fact that the electron is decelerated in the field when it approaches the turning point. As the quantum phase shift is approximately equal to the action integral along the classical trajectory, the correct choice for z_0 is such that the reflection from the wall and the reflection in the field have the same action integral,

$$\int_0^{E/F} dz\sqrt{2m^*(E - zF)} = z_0\sqrt{2m^*E}, \tag{20}$$

which gives $z_0=2E/(3F)$. When we neglect the influence of the well potential, the properly normalized scattering wave is $|k\rangle=\sqrt{2m^*/(\pi k)}\sin[k(z-z_0)]$ with wave vector $k=\sqrt{2m^*E}$, and we obtain

$$M_i(E) = \frac{m^*}{\pi k}\left[1 + \cos\left(4\frac{\sqrt{2m^*E^3}}{3F}\right)\right]|\partial_k \Psi_i(k)|^2, \tag{21}$$

where $\tilde{\Psi}_i$ denotes the Fourier transform of the initial state. We see that the modulation frequency increases with E like $\sim E^{1/2}$.

The fact that we are dealing with Airy functions rather than sine functions does not qualitatively modify the picture: at higher energies, the Airy function can be thought of as $\sim A(z)\sin(k(z)\cdot z)$ with slowly varying space dependent wave vector $k(z)$ and amplitude $A(z)$. Figure 3 compares the exact $M_i(E)$ for a Gaussian well potential with $M_i(E)$ calculated in the Born approximation, i.e., neglecting the action of the well potential on the scattering states, and with Eq. (21). The Born approximation is almost exactly reproduced by Eq. (21). However, the exact result is far overestimated by the Born approximation.

So far, our considerations were one dimensional, i.e., for a quantum well with a bias field applied perpendicular to the growth direction. For a quantum dot, the full spatial dimensions must be taken into account, which modifies the picture above. For transitions to a given direction of the continuum electron wave vector, one also observes zeros in the photoabsorption cross section, but upon integration over all direc-

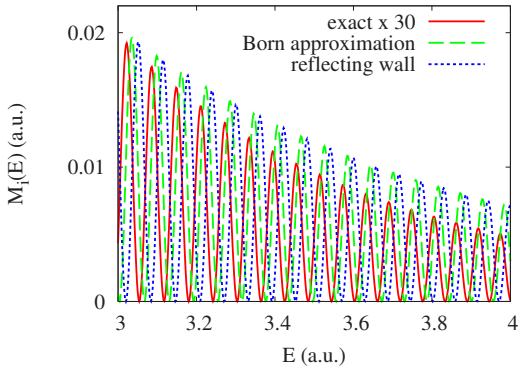

FIG. 3. (Color online) $M_i(E)$ for a Gaussian well calculated exactly (magnified by a factor of 30) in the Born approximation and with a reflecting wall at $z_0=2E/(3F)$. The modulations are reproduced correctly up to a model-dependent offset of the phase. The Born approximation and reflecting wall model closely agree, but strongly overestimate the exact $M_i(E)$ and give incorrect energy dependence.

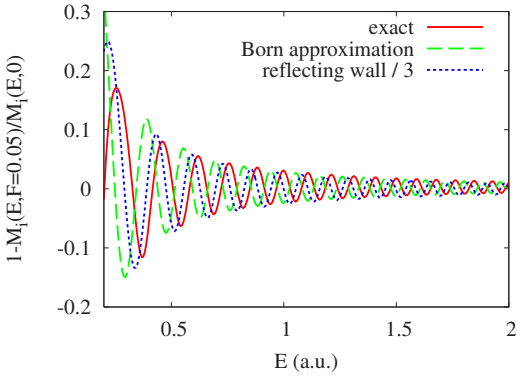

FIG. 4. (Color online) Field-induced modulations of $M_i(E)$ for a Gaussian quantum dot. Exact and Born approximation agree up to a phase offset, but the reflecting wall model (divided by 3) overestimates the modulations by a factor ≈ 3.

tions the modulations are washed out and diminish rapidly with increasing photon energy. An analytic estimate of this effect can again be obtained using the reflection from a wall at a distance $z_0=2E/(3F)$. The scattering waves with wave vector $\vec{k}$ are

$$|\vec{k}\rangle = \sqrt{\frac{m^*|\vec{k}|}{2\pi^3}} e^{i\vec{k}_\perp\cdot\vec{r}_\perp} \sin[k_z(z-z_0)], \tag{22}$$

from which one readily obtains (see the Appendix)

$$M_i(E) = \frac{m^* k^3}{2\pi^2}\left(\frac{1}{3} + \alpha\frac{\sin 2kz_0}{2kz_0}\right)|\partial_k \Psi_i(\vec{k})|^2. \tag{23}$$

Here, $\tilde{\Psi}_i$ denotes the Fourier transform of the initial state, which we have assumed to be spherically symmetric for simplicity. For the reflecting wall, we have $\alpha=1$. We see that in three dimensions the periodic modulations of the photoionization cross section become suppressed like $\sim E^{-3/2}$ with increasing photoelectron energy E. This simple formula accurately reproduces the magnitude and the modulation period of $M_i(E)$ in the Born approximation. However, to obtain the correct modulation amplitude, one must introduce the scaling factor $\alpha \approx 1/3$ (Fig. 4), which could be interpreted as moving the reflecting wall to the distance $z_0=2E/F$. A single value of z_0 fails to simultaneously account for the correct phase shift, which determines the modulation period, and the effective reflection distance, which determines the modulation amplitude. Note that these discrepancies only arise in the *modulation* of $M_i(E)$, whereas the magnitudes of $M_i(E)$ agree for the Born approximation and the reflecting wall model. However, like in the one-dimension case, both models strongly overestimate the exact $M_i(E)$.

Oscillations of the photoabsorption cross section have also been reported for atoms in strong electric fields and the basic mechanism was explained there.[21,22] In solid state physics, a related mechanism causes the well known Franz-Keldysh effect of an electric field on an optical absorption edge.[23,24]

IV. RESULTS

A. Well

We model $GaAs/Al_{0.4}Ga_{0.6}As$ quantum wells with a well potential of $V_0=-333$ meV and effective masses of $m^*=0.067$ in the well and $m^*=0.0962$ in the bulk. Without a bias field, photoabsorption is dominated by the Fabry-Pérot resonance structure of the continuum above the well. Maxima and minima of $M_i(E)$ coincide with Fabry-Pérot resonances (Fig. 5) (note the logarithmic y axis). Clearly, the energy range in this figure far exceeds the range of validity of the simple reduced mass model employed here. The calculation demonstrates that the method can reliably reproduce quantities that involve highly oscillatory parts of the continuum wave function. For physical parameters, only the energetically lowest resonance contributes significantly. Figure 6 shows the photoabsorption of the ground state of the well with a width of 4 nm. When no external field is applied, a

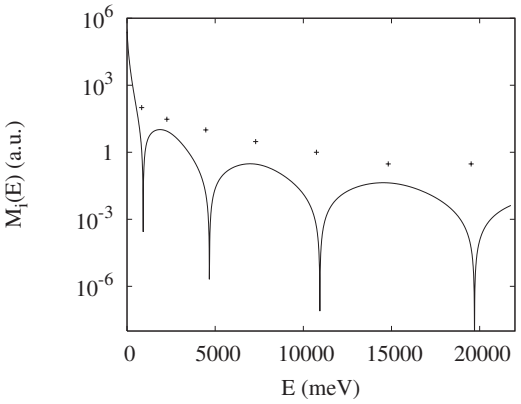

FIG. 5. $M_i(E)$ for a single quantum well without bias field. The crosses mark the Fabry-Pérot resonance energies.

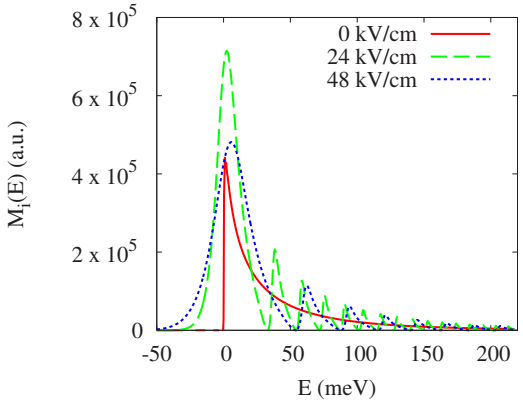

FIG. 6. (Color online) $M_i(E)$ for a single rectangular quantum well: the peak for the field-free case is the first Fabry-Pérot resonance peak in Fig. 5. With a bias field, $M_i(E)$ becomes fully modulated.

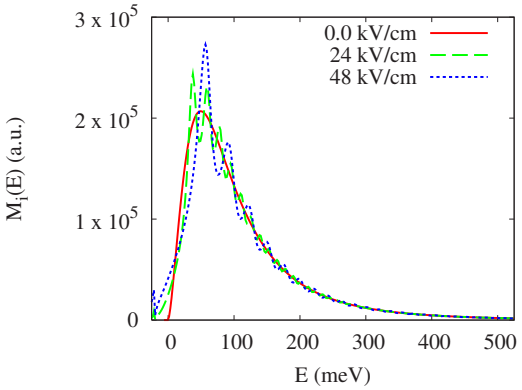

FIG. 7. (Color online) $M_i(E)$ for transitions from the ground state of a single flat quantum dot into the bulk continuum. The bulk threshold at $E=0$ becomes blurred with increasing bias field. The decay of field-induced modulations with E is slower than that for a spherically symmetric dot.

relatively smooth curve (corresponding to the lowest Fabry-Pérot resonance) is obtained. Upon the application of a field, rapid oscillations of the cross section appear, whose period increases with increasing field strength as discussed in the previous section.

One finds that the exact position and shape of the peaks are dependent on the geometry and for energies up to a few times V_0 also on the depth of the well potential. However, the modulation period depends only on the bulk parameters and on field strength and is nearly independent of the well geometry. For the present bulk reduced mass and dielectric constant, the number of zeros below energy E (in meV) at field F (in kV/cm) is given by $n=\alpha E^{3/2}/F$, with a value of $\alpha=0.12$ for all combinations of well thicknesses of 4 and 8 nm, potential depths of 333, 666, and 999 meV, and fields up to 96 kV/cm.

B. Single dot

We simulate a $Ga_{0.47}In_{0.53}As$ quantum dot ($V_0=-376$ meV, effective mass $m^*=0.041$) embedded in GaAs bulk material. The dot supports two bound states at energies $E_1=-197$ meV and $E_2=-19.5$ meV. Figure 7 gives the photoabsorption cross section for a dot with radius=8 nm and height=4 nm. Distinctive Fabry-Pérot resonances are absent in this case. As discussed earlier, modulations of the photoabsorption cross section due to a bias field decay with increasing photon energy due to integration over degenerate photoelectron momenta. As the present dot is rather flat, the decay is somewhat slower than that for the spherically symmetric dot used for the illustration in the previous section.

C. Dot in well

As the simplest case of combined QW/QD systems, we calculated photoabsorption from ground state of a dot located in the center of a well with a width of 8 nm. We use the same reduced masses, dot potential, and depth of the well potential as in the preceding sections. As energy $E=0$, we chose the GaAs conduction band edge. With this choice, the three subband thresholds of the well lie at $E=42$, 164, and 330 meV. The larger band offset in the barrier material leads to a slight increase of the ground state of the combined dot-in-well system, $E=-195$ meV (to be compared to -197 meV of the dot in bulk GaAs, Sec. IV B). The level structure is reflected in the photoabsorption shown in Fig. 8. As the field-free ground state in the dot is symmetric under $z\rightarrow -z$, without a bias field the first dipole-allowed subband states are the odd states starting from the threshold energy of 164 meV. When the field is turned on, it breaks the reflection symmetry with respect to z and the transitions to the lowest subband starting from $E=42$ meV become dipole allowed. There appears a very pronounced peak in the photoabsorption at a subband energy $E=137$ meV, which exceeds the value at the second subband threshold by several orders of magnitude. This peak is due to a resonant state induced by the dot potential in the first well subband. It is completely absent when the influence of the dot potential on the subband continuum is neglected (see Fig. 9 below). A similar behavior is observed at 330 meV, where the symmetry of the third well subband becomes lifted and a peak in the photoabsorp-

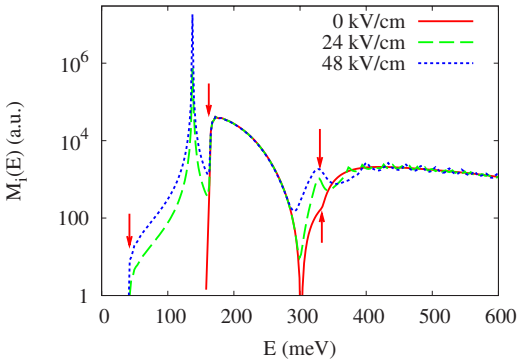

FIG. 8. (Color online) $M_i(E)$ for a quantum dot embedded in a quantum well without bias field and with bias fields of 24 and 48 kV/cm. The arrows mark the field-free subband (down arrows) and bulk (up arrow) thresholds.

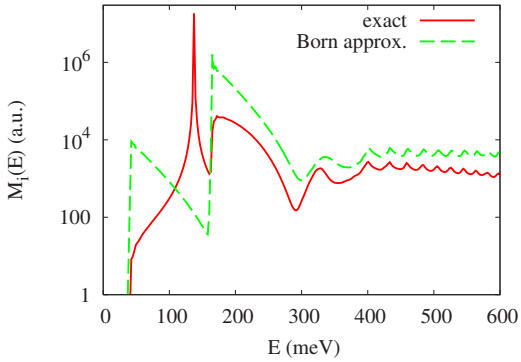

FIG. 9. (Color online) Exact $M_i(E)$ vs Born approximation. System parameters are the same as in Fig. 8 for a field of 48 kV/cm. Born approximation overestimates $M_i(E)$ by $O(30)$ and misses the sharp peak in the first subband.

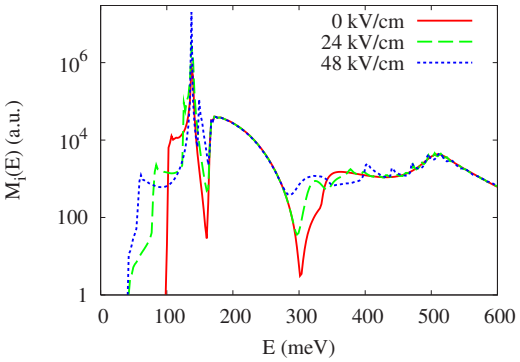

FIG. 11. (Color online) Quantum dot within three wells separated by a narrow barrier. Transitions at energies of 50 meV are enhanced comparing to Fig. 10 due to stronger coupling to adjacent wells.

tion into the third subband grows with the bias field.

Just below the third subband threshold, a zero occurs in $M_i(E)$ at $E \approx 300$ meV. It is due to effectively one-dimensional nature of the subband continuum in the cylindrically symmetric system. Without a bias field and when we neglect the influence of the dot potential, the wave functions of the second subband are

$$|k_\rho, 2\rangle \propto J_n(k_\rho \rho)\Phi_2(z), \tag{24}$$

where J_n is the nth Bessel function and $\Phi_2(z)$ denotes the second well state. With a cylindrically symmetric initial state $\Psi_i(\rho,z)$, transitions occur only to the $n=0$ states. The zero occurs as the radial wave vector k_ρ increases and the nodes of $J_0(k_\rho\rho)$ move across the support of $\Psi_i(\rho,z)$, causing sign changes of the matrix element. The mechanism remains unaltered when the exact scattering wave functions are used instead of Eq. (24). When a bias field is switched on, the exact zero in the absorption cross section is reduced to a dip. This is because the third subband lies rather near the bulk threshold and experiences a significant dc Stark shift of $\Delta E = 4.6$ meV and also acquires a width of $\Gamma = 29$ meV, which covers the zero of the field-free case.

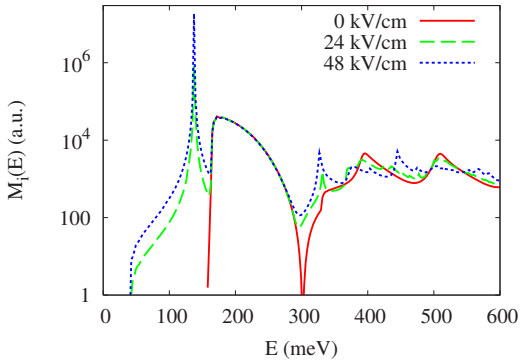

FIG. 10. (Color online) $M_i(E)$ for a quantum dot within three equidistant wells.

Field-induced modulations of absorption appear only above the bulk threshold, where the wave functions have continuous character also in the z direction.

The general characteristics of the spectra can be deduced making the Born approximation for the continuum states as discussed above, i.e., by ignoring the impact of the dot on the continua. However, quantitatively the results deviate dramatically and obviously dot-induced resonances cannot be reproduced. To demonstrate this, we made a calculation where we use the Born approximation for the continuum states, i.e., we calculate the resolvent in Eq. (3) for the Hamiltonian without the dot potential

$$H_{well} = -\frac{1}{2m^*(\rho,z)}\left[\frac{1}{\rho}\frac{\partial}{\partial\rho}\rho\frac{\partial}{\partial\rho} + \frac{\partial^2}{\partial z^2}\right] + V_{well}(z) + ezF. \tag{25}$$

Figure 9 compares the field-free exact photoionization with the Born approximation. In general, the Born results strongly overestimate the actual cross sections. This is due to the higher electron velocity and correspondingly lower amplitude and stronger oscillatory behavior of the scattering wave functions in the region of the dot potential as compared to the plane waves of the Born approximation.

D. Dot in multiple wells

For Figs. 10–12, additional wells and barriers have been added keeping the same reduced masses and potential depth as before. Figure 10 shows absorption for a three-well structure with wells of width 8 nm separated by barriers of 8 nm added to either side of the central dot-in-well system. The influence of adjacent wells is small and differences mainly arise due to modification of the bulk continuum. As in the single well case, the bias field enables otherwise forbidden transitions due to symmetry breaking. Above the bulk threshold, one again sees field-induced modulations of the photoabsorption cross section.

Figures 11 and 12 show systems of a dot within multiple wells, where the width of the barriers and outer wells has been reduced to 4 nm (with only the middle well at 8 nm).

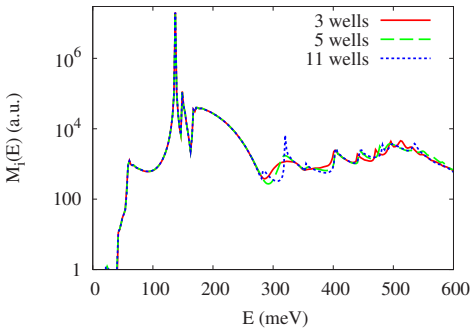

FIG. 12. (Color online) Quantum dot within 3, 5, and 11 wells at $F=48$ kV/cm. Only minor differences of $M_i(E)$ near and in the bulk continuum can be seen.

The graph in Fig. 11 (three wells) is similar to the one above (the transition to the first z-bound state is suppressed in the field-free case). However, the low energy regime shows remarkable modifications as compared to Fig. 10 due to the coupling to the neighboring wells. The threshold of the second subband of the field-free triple-well system lies at 102 meV and is Stark shifted to 57 meV at a field of 48 kV/cm. In addition, we notice a sharpening of the peaks in the bulk continuum with an increasing number of wells.

V. CONCLUSION

In this paper, we used resolvent formalism and complex scaling for the numerical calculation of photoabsorption cross sections. These methods were found to be efficient and well converging particularly for bound-continuum transitions in the case of an external electric field.

The cross sections are dominated by the shape of the particular heterostructure, which determines the Fabry-Pérot resonances and subband thresholds, and by bias-field-induced modulations of the photoabsorption cross section. The modulations are complete for transitions from subband states into the bulk, whereas they are only significant near threshold of a dot-bulk transition and decay rapidly at higher energies. A specific feature of dot-subband transitions in a QD/QW system are zeros in the photoabsorption that can appear due to the reduced dimensionality of the subband continuum. When a bias field is applied in the growth direction of the QD/QW system, field-induced modulations appear only above the bulk threshold.

We have demonstrated that the density of the field-induced modulations is largely independent of a specific well structure, which allows us to determine the local bias field from a measurement of the photoabsorption.

We also showed that the Born approximation for realistic system parameters seriously overestimates the photoionization cross sections and, maybe more severely, misses important features such as strong resonances in the subbands that are induced by the dot potential.

For the transition of an electron from the dot into the subbands of a superlattice, the most significant structures arise from the energy thresholds of the subbands. In our geometry, these were basically defined by the single well into which the dot has been embedded. Only for narrow barriers can the nearest adjacent wells modify the photoabsorption spectrum. The addition of further wells produces only minor distortions near and above the bulk threshold.

ACKNOWLEDGMENTS

We are grateful to G. Strasser and K. Unterrainer for helpful discussion. This work was supported by the Austrian Research Fund, Projects Nos. F01115 and F01611.

APPENDIX: DERIVATION OF EQUATION (23)

We approximate the wave in the electric field F by a plane wave reflected from a solid wall at a distance z_0,

$$|\vec{k}\rangle = Ne^{i\vec{k}_\perp\cdot\vec{r}_\perp}\sin[k_z(z-z_0)], \tag{A1}$$

with the normalization

$$N = \sqrt{\frac{m^*|\vec{k}|}{2\pi^3}}.$$

The dipole matrix element from an initial state $|\Psi_i\rangle$ then is

$$\langle\vec{k}|z|\Psi_i\rangle = \frac{N}{2i}\int d^{(3)}r\Psi_i(\vec{r})z \times[e^{-i(\vec{k}_\perp\cdot\vec{r}_\perp-k_zz)}e^{-ik_zz_0} - e^{-i(\vec{k}_\perp\cdot\vec{r}_\perp+k_zz)}e^{ik_zz_0}]. \tag{A2}$$

If we assume that the initial state is symmetric with respect to reflections of z, $\Psi(\vec{r}_\perp,z)=\Psi(\vec{r}_\perp,-z)$, the integral (A2) becomes

$$\frac{N}{i}\cos(k_zz_0)\int d^{(3)}re^{-i(\vec{k}\cdot\vec{r})}z\Psi_i(\vec{r}), \tag{A3}$$

which can be written using the Fourier transform $\tilde{\Psi}_i(\vec{k})$ as

$$-N\cos(k_zz_0)\frac{\partial}{\partial k_z}\Psi_i(\vec{k}). \tag{A4}$$

We simplify the integration over angles by assuming that Ψ_i is spherically symmetric, $\partial_{k_z}\tilde{\Psi}_i=\eta\partial_k\tilde{\Psi}_i$. The angles of $|\vec{k}\rangle$ are restricted to the half-sphere, which results in

$$\begin{aligned}
&k^2\int_0^{2\pi}d\varphi_k\int_0^1 d\eta|\langle\vec{k}|z|\Psi_i\rangle|^2 \\
&= 2\pi N^2k^2\int_0^1 d\eta\eta^2[\cos(\eta kz_0)]^2|\partial_k\Psi_i(\vec{k})|^2 \\
&= \pi N^2k^2\int_0^1 d\eta\eta^2[1+\cos(2\eta kz_0)]|\partial_k\Psi_i(\vec{k})|^2 \\
&= \frac{m^*k^3}{2\pi^2}|\partial_k\Psi_i(\vec{k})|^2 \\
&\times\left[\frac{1}{3}+\frac{\sin 2kz_0}{2kz_0}+\frac{2\cos 2kz_0}{(2kz_0)^2}-\frac{2\sin 2kz_0}{(2kz_0)^3}\right].
\end{aligned} \tag{A5}$$

Keeping only the leading terms of the oscillatory part, we arrive at Eq. (23).

*scrinzi@tuwien.ac.at

[1] S. Anders, L. Rebohle, F. F. Schrey, W. Schrenk, K. Unterrainer, and G. Strasser, Appl. Phys. Lett. **82**, 3862 (2003).
[2] S. Raghavan, D. Forman, P. Hill, N. R. Weisse-Bernstein, G. von Winckel, P. Rotella, and S. Krishna, J. Appl. Phys. **96**, 1036 (2004).
[3] G. Ariyawansa, A. G. U. Perera, G. S. Raghavan, G. von Winckel, A. Stintz, and S. Krishna, IEEE Photonics Technol. Lett. **17**, 1064 (2005).
[4] S. Krishna, J. Phys. D **38**, 2142 (2005).
[5] F. F. Schrey, L. Rebohle, T. Müller, G. Strasser, K. Unterrainer, D. P. Nguyen, N. Regnault, R. Ferreira, and G. Bastard, Phys. Rev. B **72**, 155310 (2005).
[6] C. Pryor, Phys. Rev. B **57**, 7190 (1998).
[7] O. Stier, M. Grundmann, and D. Bimberg, Phys. Rev. B **59**, 5688 (1999).
[8] N. Vukmirovic, D. Indjin, V. D. Jovanovic, Z. Ikonic, and P. Harrison, Phys. Rev. B **72**, 075356 (2005).
[9] L.-W. Wang, J. Kim, and A. Zunger, Phys. Rev. B **59**, 5678 (1999).
[10] A. Amtout, S. Raghavan, P. Rotella, G. von Winckel, A. Stintz, and S. Krishnaa, J. Appl. Phys. **96**, 3782 (2004).
[11] R. Buczko and F. Bassani, Phys. Rev. B **54**, 2667 (1996).
[12] P. Lelong, S. W. Lee, K. Hirakawa, and H. Sakaki, Physica E (Amsterdam) **7**, 174 (2000).
[13] A. Vasanelli, R. Ferreira, H. Sakaki, and G. Bastard, Solid State Commun. **118**, 459 (2001).
[14] D. P. Nguyen, N. Regnault, R. Ferreira, and G. Bastard, Phys. Rev. B **71**, 245329 (2005).
[15] W. Sheng and J.-P. Leburton, Phys. Rev. B **64**, 153302 (2001).
[16] G. Bester and A. Zunger, Phys. Rev. B **72**, 165334 (2005).
[17] N. Vukmirović, D. Indjin, Z. Ikonić, and P. Harrison, Appl. Phys. Lett. **88**, 251107 (2006).
[18] C. W. McCurdy, T. N. Rescigno, W. A. Isaacs, and D. E. Manolopoulos, Phys. Rev. A **57**, 3511 (1998).
[19] A. Scrinzi and N. Elander, J. Chem. Phys. **98**, 3866 (1993).
[20] M. Reed and B. Simon, *Methods of Modern Mathematical Physics* (Academic, New York, 1982), Vol. IV, p. 183.
[21] H. Rottke and K. H. Welge, Phys. Rev. A **33**, 301 (1986).
[22] J. Gao, J. B. Delos, and M. Baruch, Phys. Rev. A **46**, 1449 (1992).
[23] W. Franz, Z. Naturforschung **13a**, 484 (1958).
[24] L. V. Keldysh, Sov. Phys. JETP **34**, 788 (1958).